Sintering of calcium phosphates with a femtosecond pulsed laser for hard tissue engineering

A.D. Anastasiou [a,*], C.L. Thomson [b], S.A. Hussain [b], T.J. Edwards [b], S. Strafford [c], M. Malinowski [c], R. Mathieson [a], C.T.A. Brown [b], A.P. Brown [a], M.S. Duggal [c], A. Jha [a]

[a] The Institute for Materials Research, School of Chemical and Process Engineering, University of Leeds, Leeds LS2 9JT, UK
[b] SUPA, School of Physics and Astronomy, University of St Andrews, North Haugh, St Andrews, Fife, KY16 9SS, UK
[c] Leeds Dental School, Worsley Building, University of Leeds, Leeds LS2 9JT, UK

ABSTRACT

Direct laser sintering on hard tissues is likely to open new pathways for personalised medicine. To minimise irradiation damage of the surrounding soft tissues, lasers operating at wavelengths that are 'safe' for the tissues and biomaterials with improved optical properties are required. In this work laser sintering is demonstrated with the use of an ultrafast, femtosecond (100 fs) pulsed laser operating at a wavelength of 1045 nm and two existing calcium phosphate minerals (brushite and hydroxyapatite) which have been improved after doping with iron (10 mol%). Femtosecond laser irradiation caused transformation of the Fe^{3+}-doped brushite and Fe^{3+}-doped HAp samples into β-calcium pyrophosphate and calcium-iron-phosphate, respectively, with simultaneous evidence for microstructural sintering and densification. After estimating the temperature profile at the surface of the samples we suggest that soft tissues over 500 μm from the irradiated zone would be safe from thermal damage. This novel laser processing provides a means to control the phase constitution and the morphology of the finished surfaces. The porous structure of β-pyrophosphate might be suitable for applications in bone regeneration by supporting osteogenic cell activity while, the densified Fe^{3+}-rich calcium-iron-phosphate may be promising for applications like dental enamel restoration.

1. Introduction

Personalised or precision medicine and near patient manufacturing are emerging concepts which may influence and define the treatment pathway for certain diseases; e.g. in dentistry and regenerative tissue engineering. Although the idea of "personalised medicine" dates back to the age of Hippocrates, it was only at the beginning of the 19th century when technological achievements in the fields of microscopy, biomedical sensing, imaging and manufacturing allowed clinicians to begin to implement these concepts [1]. Restorative and reconstructive surgery is a critically important area of personalised medicine with the potential to design and manufacture individual bone grafts that depend on the needs of each patient (clinical and environmental). The most efficient way, to date, to achieve this is through Rapid Prototyping (RP) technologies with Selective Laser Sintering (SLS) being one of the most developed and successfully applied methodologies [2].

Guided by the principles of personalised medicine and based on the fundamentals of SLS the long term goal of our research is to develop a procedure where direct laser sintering, densification and bonding of a layer of fresh biomaterial on hard tissues (i.e. bone and teeth) can be achieved. A technique like this could find a unique space in restorative and reconstructive surgery for surface engineering small bone and tooth defects as well as coating existing implants and scaffolds. To accomplish this, the mineral laser sintering of hard-tissue must be made safe for patients and clinicians by minimizing any collateral damage to the surrounding soft tissues. While the effects of photochemical laser-tissue interactions can be easily avoided by decreasing the total irradiation time, it seems that the key parameter for minimizing thermal interactions and the damage of biological tissues is pulse duration. According to Niemz [3] pulses with duration >1 μs are often associated with measurable thermal effects, whereas for pulse durations <1 μs and for moderate repetition rates (10–100 kHz), thermal effects usually become negligible. More broadly, the extent and degree of tissue damage during interaction with a laser beam depends both on the irradiation parameters of the laser (e.g. wavelength, average energy, pulse duration and exposure time) and on the optical properties of the tissues (e.g. absorption and scattering coefficients at the irradiation wavelength). The latter are determined by the presence of proteins, such as melanin and haemoglobin, which are responsible for absorption in the UV–visible section of the electromagnetic spectrum and the presence of free water and hydroxyl (OH^-) group molecules, which are critical for absorption

at visible and infrared regions of the spectrum. Taking all these factors into account, we suggest that optimisation for direct sintering on hard tissue would require a short pulsed laser, emitting at wavelengths between the visible and near infrared, where the absorption properties of melanin (>700 nm) and haemoglobin (>600 nm) are neglected and where water's absorption coefficient is still low [4].

In our investigation, we have selected a femtosecond laser regime for thermal management, because the short pulse duration helps control dissipation of absorbed energy while high repetition rates minimise the energy delivered per pulse. So far there are relatively few reports on the utilisation of pulsed lasers for SLS and these have been restricted to the investigation of metal powders (e.g. [5]) while most of the recent work on SLS manufacturing of calcium phosphate tissue scaffolds have been focused on continuous wave CO_2 lasers emitting at 10.6 μm (e.g. [6,7]). In addition, Antonov et al. [8] and Antonov et al. [9] have utilised a CW diode laser emitting at 970 nm and 1027 nm respectively in order to construct bioactive scaffolds while a similar laser type was used also by O'Flynn and Stanton [10] to investigate the sintering of a bioactive glass ceramic for potential biomedical applications. There are however recent promising, reports of femtosecond pulsed lasers being used for the fixation of calcium phosphate mineral particles on titanium alloy implants (i.e. [11,12]) and of calcium phosphate coatings on dental enamel surfaces [13].

Various forms of calcium phosphates have been successfully used for SLS applications because of the compositional and structural similarity of calcium phosphate (CaPs) materials to that in human bone and teeth (with use as bone replacements and scaffolds, coatings for orthopaedic devices and dental implants etc.). In the present study two different types of calcium phosphates were investigated, namely hydroxyapatite [HAP: $Ca_{10}(PO_4)_6(OH)_2$] and brushite (DCPD: $CaHPO_4 \cdot 2H_2O$). Hydroxyapatite [HAP: $Ca_{10}(PO_4)_6(OH)_2$] is the most popular of the calcium phosphates in clinical practice since it is the most similar material to the mineral component of bone and teeth. However its application is limited due to a number of factors like brittleness and an extremely low rate of bioresorption (e.g. [14]). As a result there are attempts to develop new grafting materials more soluble in physiological conditions (for example [15]). One of these materials is the mineral brushite (DCPD: $CaHPO_4 \cdot 2H_2O$) which can occur as an intermediate in bone mineralisation and during the dissolution of enamel in acids [16]. The advantage of brushite over hydroxyapatite is its ability to be resorbed under physiological conditions while, its properties (i.e. mechanical, bioactivity) can be improved through doping with various ions [17]. In this work calcium phosphate materials doped with iron ions (Fe^{3+}) will be demonstrated, specifically to improve the linear absorption of femtosecond pulsed laser irradiation at the near IR wavelength. Notwithstanding the optical reasons for doping, adding iron to calcium phosphate biomaterials can also increase osteoconductive properties which are critical for tissue engineering applications [18].

In summary, the aim of the present work is to investigate the potential use of a femtosecond laser for sintering of calcium phosphate biomaterials and to demonstrate that sintering may be achieved at emerging, commercial fs pulsed-laser wavelengths (e.g. at 1045 nm) using significantly lower average power of say, 0.4 W investigated herein, than the current commercial Q-switched laser powers. Additionally, we demonstrate operating parameters which could be used for laser sintering of an optimized biomaterial layer on existing implants or hard tissue defect, enabling the design of new, restorative coating procedures.

2. Materials and methods

2.1. Materials synthesis

The procedure described by Elmadani et al. [13] was followed for the synthesis of brushite (DCPD-UN). 200 mL of a 0.1 M $Ca(NO_3)_2 \cdot 4H_2O$ aqueous solution was heated to 37 °C, then a 0.1 M $(NH_4)_3PO_4$ solution

(200 mL) was added drop by drop. The final mixture was left under continuous stirring at 37 °C for 2 h, then left settle for 1 h to allow precipitation. During these process steps, the top of the beaker was sealed with aluminium foil to exclude the CO_2 ingress into the phosphated mineral solution. The brushite crystals which formed were collected on a filter paper (Whatman grade 44 with pores of 1 μm), washed several times with distilled water and dried for 24 h at 70 °C. Synthesis of the Fe-doped brushite (DCPD-Fe) followed a similar route, however before the addition of the $(NH_4)_3PO_4$ solution, 10 mol% $Fe(NO_3)_3 \cdot 9H_2O$ was added to the calcium nitrate solution.

A reagent grade commercial hydroxyapatite powder was used for the undoped HAP (HAP-UN; Sigma Aldrich® 21223). For the synthesis of iron (Fe^{3+}) doped hydroxyapatite (HAP-Fe), 200 mL of a 0.1 M $Ca(NO_3)_2 \cdot 4H_2O$ was prepared to which 10 mol% $Fe(NO_3)_3 \cdot 9H_2O$ was added. The aqueous solution was heated to 37 °C and 200 mL of a 0.1 M $(NH_4)_3PO_4$ solution added dropwise under continuous stirring. During the whole procedure small quantities of NaOH solution (0.1 M) were added to the mixture to maintain a total pH higher than 9. After 2 h at 37 °C the solution was allowed to settle in order for precipitation to take place. As in the case of the brushite minerals, the (HAP-Fe) crystals were collected on a filter paper and dried for 24 h at 70 °C. The powder was calcined at 650 °C for 12 h. The materials used in the following experiments are presented in Table 1.

To test the interaction of the materials with the laser, powder pellets were pressed in a die with diameter of 13 mm. For each pellet approximately 0.25 g of the corresponding powder was filled inside the die before pressing with a load of 7 ton for 30 min.

2.2. Characterisation methods

The crystal structure and purity of the synthesized mineral phases were analyzed by X-ray powder diffraction using a Philips X'Pert MPD, with monochromatic Cu Kα radiation (0.154098 nm). The diffractometer step size was 0.065° and the 2θ scanning range was from 10° to 60°, such that data were collected over a period of approximately 25 min with a scan speed of 0.014° s^{-1}. Both the powder samples and the sintered pellets were measured by X-ray diffraction with these settings.

Scanning electron microscopy (SEM, a Hitachi SU8230 1–30 kV cold field emission gun) was used to investigate the size and shape of the powder crystals and for identification of physical and chemical changes induced by laser irradiation. The microscope was equipped with an Oxford Instruments 80 mm^2 SD detector for energy dispersive X-ray (EDX) spectrometry with Aztec processing software to enable analysis of any compositional changes in the mineral phases to be quantified (by a standardless routine). Since calcium phosphate minerals have poor electrical conductivity, prior to SEM and EDX analysis each sample was coated with a 5 nm thick layer of platinum and then vacuum cleaned for 10 min.

A Simultaneous Thermal Analyser (PerkinElmer®, STA 8000) with the capability of acquiring thermogravimetric analysis (TGA) and differential scanning calorimetry (DSC) was used to investigate the reactions and phase changes which take place during the heating of the materials. All thermal experiments were carried out over a temperature range from 40 to 1500 °C and at a heating rate of 20 °C per min.

A UV–VIS spectrometer (Perkin Elmer, LAMBDA 950) equipped with a 60 mm integrating sphere module was used to measure the reflectivity of the materials. Measurements were performed on the

Table 1
Materials used during the experiments.

Code	Mineral	Fe mol%
DCPD-UN	Brushite	–
DCPD-Fe	Brushite	10
HAP-UN	Hydroxyapatite	–
HAP-Fe	Hydroxyapatite	10

non-irradiated pressed pellets for wavelengths ranging from 250 to 2000 nm.

2.3. Laser sintering experiments

The fs-laser irradiation experiments were performed with an ultrafast, pulsed source from a single crystal cavity of Yb:KGW (developed in-house at St Andrews). Once the laser cavity was optimized, typical pulse duration of the mode-locked cavity was controlled to be between 130 and 190 fs with an emission wavelength at 1045 nm and a repetition rate of 1 GHz. The phosphate mineral pellets were placed on a 3-axis motorised translation stage, controlled by a LabView routine in order to have zigzag irradiation patterns, as presented in Fig. 1. The total irradiated area of the pressed pellets was a rectangular section of 6×4 mm^2, which was large enough to characterize any phase changes by X-ray powder diffraction. During the laser irradiation experiments the average laser power was adjusted to 0.40 W (measured at the output of the source), the scanning velocity was 100 μm/s and the spot diameter was 30 μm. These beam characteristics produced a pulse energy of ~0.4 nJ and each spot was exposed for a total of 0.3 s.

3. Results

3.1. Characterisation of the synthesized materials

Diffraction patterns of the brushite and Fe^{3+} doped brushite powders before laser irradiation are presented in Fig. 2a and compared with the reference pattern of brushite (JCPDS-01-074-6549). All the major peaks in both patterns match satisfactorily to the reference, indicating that the synthesized calcium phosphate may be considered to be ~98% brushite (with minor quantities of monetite evident by the (0 2 0) peak at 26.5°). The diffraction peaks of the DCPD-Fe sample are however systematically shifted by 0.05 to 0.2° to larger 2θ indicating a reduction in lattice volume suggesting that the Fe^{3+}-ions may have been incorporated into the brushite lattice. It is also evident that the relative intensity of the brushite (0 2 0) and (0 4 0) peaks (at 2θ = 11.56° and 2θ = 23.51° respectively) are much higher than those in the reference pattern. These planes lie in the same zone axis as the (0 1 0) plane and so we can assume that the different reflexion intensities are due to texture of the crystals and that the (0 1 0) plane is the preferred habit of the brushite powder. After laser irradiation the XRD patterns for both materials changed dramatically, the brushite transformed into β-pyrophosphate (β-$Ca_2P_2O_7$), since all diffraction peaks in the irradiated sample match with the peaks in the corresponding reference pattern (JCPDS-04-009-8733 and Fig. 2b). Residual brushite (0 2 0) and (0 4 0) peaks are still present at 2θ = 11.56° and 2θ = 23.51° respectively, and given that the penetration depth of the X-ray beam ranges from 20 to 120 μm (depending on the Bragg angle, 2θ), it is likely

that while there may be complete transformation of the material at the surface of the pellet, some of the underlying mineral remains unaltered. Analysis of the cross section of the pellet by SEM supports this conclusion with clear evidence that morphological changes in crystals have occurred only as deep as 50 μm below the surface (see below Fig. 6f). The comparison of the X-ray diffraction patterns of the un-doped and the doped material shows that the only difference between the post irradiation patterns may be in the relative diffraction intensity of the β-pyrophosphate (0 0 8) peak (at 2θ = 29.7°) in comparison with the principle brushite (0 2 0) peak (at 2θ = 11.56°). This could be attributed to texture disturbance upon laser induced remineralisation of the Fe doped material.

Numerous workers have investigated the transformations of brushite during heating (e.g. [19,20]) and the results reported herein are consistent with these reports. The first transformation upon heating DCPD-UN occurs at 196 °C (Fig. 3), when brushite loses two molecules of water and transforms into monetite ($CaHPO_4$) following the reaction in Eq. (1).

Further heating, to 474 °C, results in the loss of 1/2 H_2O from the formula unit of monetite and leads to the formation of γ-pyrophosphate (γ-$Ca_2P_2O_7$) (Eq. (2)). Pyrophosphates are compounds with dichromate structure and depending on the firing temperature they might exist in three different forms [21]. Thus at 813 °C the β form is obtained which eventually changes at 1293 °C to α-$Ca_2P_2O_7$. The latter is not very stable and in many cases transforms back to the β form during cooling. The melting point is identified at 1380 °C (Fig. 3).

$$2CaHPO_4 \cdot 2H_2O \overset{196\,°C}{\Longrightarrow} 4H_2O + 2CaHPO_4 \tag{1}$$

$$2CaHPO_4 \overset{474\,°C}{\Longrightarrow} H_2O + Ca_2P_2O_7 \tag{2}$$

For the Fe^{3+}-doped brushite it was found that these transformations shift to lower temperature (Table 2). The transformation temperature of β-pyrophosphate to the α-form has been reduced by 212 °C (from 1293 to 1012 °C) while, the melting point reduced by 108 °C (from 1380 to 1272°C). This might be expected since cationic substitutions in apatites have been reported to destabilise the structure upon heating and are known to reduce decomposition temperatures [22].

Thus, assuming that the observed transformation of irradiated brushite (Fig. 2) is a thermal process and accounting for the measured temperature required for β-pyrophosphate formation (Fig. 3), we propose that during fs-pulsed laser irradiation the local temperature on the surface may rise to between 813 °C and 1293 °C within the 0.3 s of irradiation.

The X-ray diffraction patterns of the non-irradiated HAP-UN and HAP-Fe are consistent with the reference pattern of hydroxyapatite (JCPDS-01-074-9762 in Fig. 4a). The behaviour upon laser irradiation
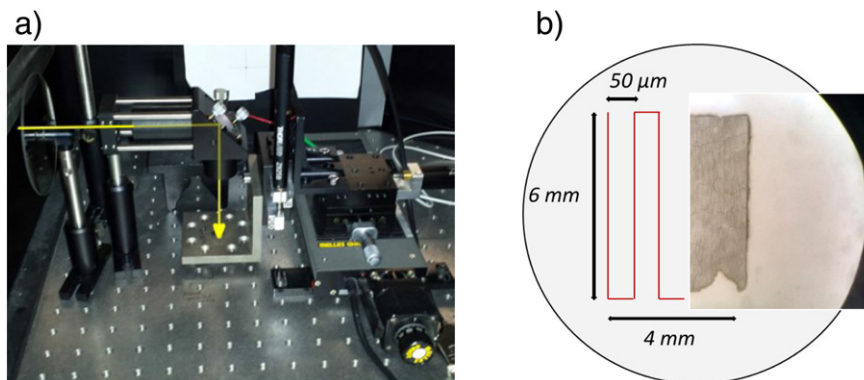
Fig. 1. a) Layout of the Yb-KGW crystal based 1 GHz laser set up; b) laser irradiation pattern (magnified red lines) and optical image (darker area has been irradiated) of the surface of a pressed calcium phosphate pellet.
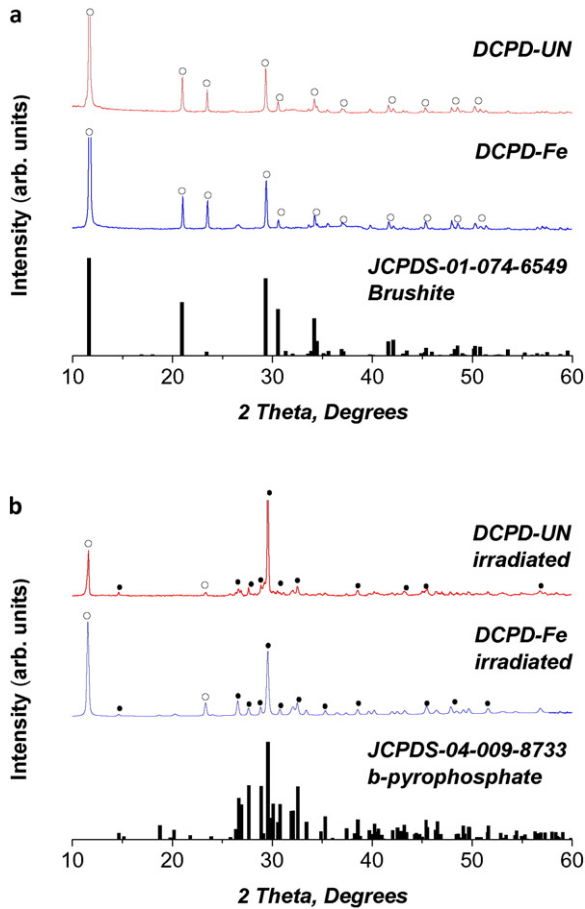
Fig. 2. A comparison of X-ray diffraction patterns of brushite and 10 mol% Fe doped brushite pellets; a) before laser irradiation; b) after laser irradiation; with indexing to the JCPDS reference files of brushite (○) in a) and β-pyrophosphate (•) in b).

Table 2
Transformation temperatures for the un-doped and the Fe doped brushite.

Transformation	DCPD-UN, °C	DCPD-Fe, °C
Brushite to monetite	196	200
Monetite to γ-$Ca_2P_2O_7$	474	459
γ-$Ca_2P_2O_7$ to β-$Ca_2P_2O_7$	813	720
β-$Ca_2P_2O_7$ to α-$Ca_2P_2O_7$	1293	1012
Melting point	1380	1272

state synthesis of calcium iron phosphate ($Ca_9Fe(PO_4)_7$) using Fe_2O_3, $CaCO_3$ and $NH_4H_2PO_4$ precursors is nearly 1000 °C.

As indicated above, doping with Fe^{3+}-ions has changed the optical properties of the calcium phosphate materials. This is also evident by reflectivity changes of the Fe-doped materials compared to the un-doped brushite (Fig. 5). At the 1045 nm fs-pulsed laser irradiation wavelength, the reflectivity for the un-doped brushite is 84%, which drops to 70% for the Fe^{3+}-doped brushite and 36% for the Fe^{3+}-doped hydroxyapatite, indicating that doping with Fe^{3+} ions increases photon absorptivity at this wavelength.

SEM images of the microstructures of the irradiated and non-irradiated brushite pellet are compared in Fig. 6. The outlines of the original brushite platelets (Fig. 6a) are still evident in the images of the irradiated pellet (Fig. 6b and c). However the high magnification images show alteration of the surface of individual particles to a porous or micro-cracked microstructure, following the transformation of brushite to β-calcium pyrophosphate (Fig. 6b and c). The presence of irregular porosity and significant cracks in the intergranular regions indicates that the un-doped material has not sintered after fs-pulsed laser

is different for these two HA-based materials from that for brushite. The XRD pattern of un-doped hydroxyapatite remained unchanged after fs-laser irradiation. However the Fe^{3+} doped mineral transformed into calcium iron phosphate ($Ca_9Fe(PO_4)_7$), as can be seen in Fig. 4b. Lazoryak et al. [23] show that the temperature required for the solid
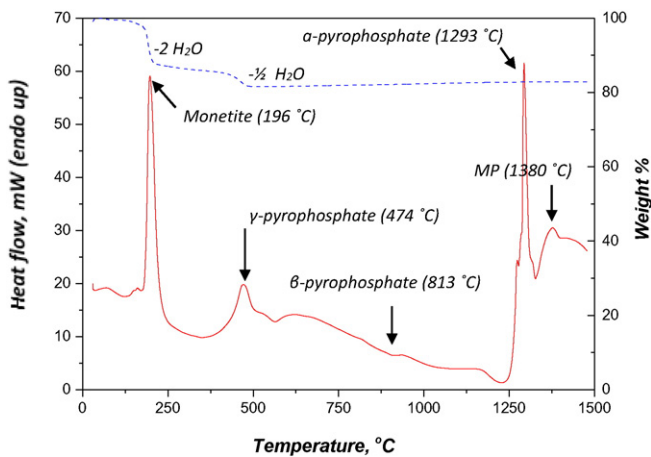
Fig. 3. Thermal analysis of brushite (DCPD-UN) and identification of the phase transformation temperatures (the DSC curve is shown in red and values reported on the LH y-axis while the TGA curve is shown in blue and values reported on the RH y-axis).

Fig. 4. X-ray diffraction patterns of hydroxyapatite and 10% Fe doped hydroxyapatite; a) before laser irradiation; b) after laser irradiation with indexing to the reference patterns for the main phase of hydroxyapatite (•) in a) and calcium-iron-phosphate (○) in b). (*) denotes the monetite (0 2 0) peak in the hydroxyapatite sample.
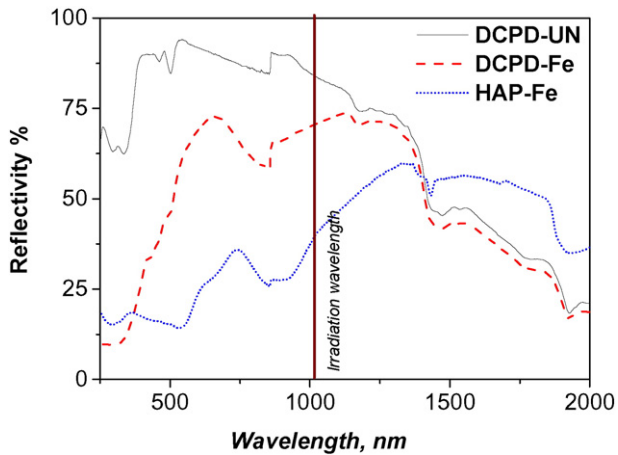
Fig. 5. Reflectivity measurements from the surface of the pressed calcium phosphate pellets. Results for brushite (DCPD-UN), Fe^{3+}-doped brushite (DCPD-Fe) and Fe-doped hydroxyapatite (HAP-Fe) show that Fe^{3+}-doping increases the absorption at 1045 nm.

irradiation. The apparent physical changes in the microstructure are likely to be due to the loss of water of crystallisation above 190 °C when brushite starts transforming to monetite and then above 470 °C on further transformation to pyrophosphate.

Comparing the Fe^{3+}-doped brushite pellet with un-doped brushite pellet (Fig. 6), it is apparent that the irradiated Fe^{3+}-doped material has transformed much more dramatically than the un-doped counterpart. There is no evidence of the original acicular crystal outlines of brushite after irradiation, instead a homogenous densified material with pores and micro-cracks are randomly distributed across the surface of the pellet (Fig 6e). Porosity and densification were also verified by SEM imaging of the cross-section of the irradiated Fe-doped brushite pellet in which internal pores of 20–40 μm are visible (Fig. 6f). The formation of these large pores may be due to the non-uniform distribution of particles and porosity in the initial material. In such circumstances, when differential sintering and densification takes place, particles may move to cause the generation of pores larger than the initial ones and so as sintering proceeds pore opening can be observed [24]. The difference in packing density between the sintered/transformed area and the underlying, intact, un-irradiated material is also obvious while the depth of sintering reaches as far as 60–65 μm below the surface.

The only material unaltered by laser irradiation is the un-doped hydroxyapatite (Fig. 7b). Although discoloration of the irradiated area has been observed, the HAP crystals seem to be intact, retaining the original morphology (comparing Fig. 7a and c). Moreover, on that sample there is no indication of sintering or a phase change, consistent with the X-ray diffraction analysis (Fig. 3). On the other hand the fs-pulsed laser induced morphological and structural changes of the Fe^{3+}-doped HAP pellet are radical when imaged by SEM (Fig. 7e). A dense, homogeneous
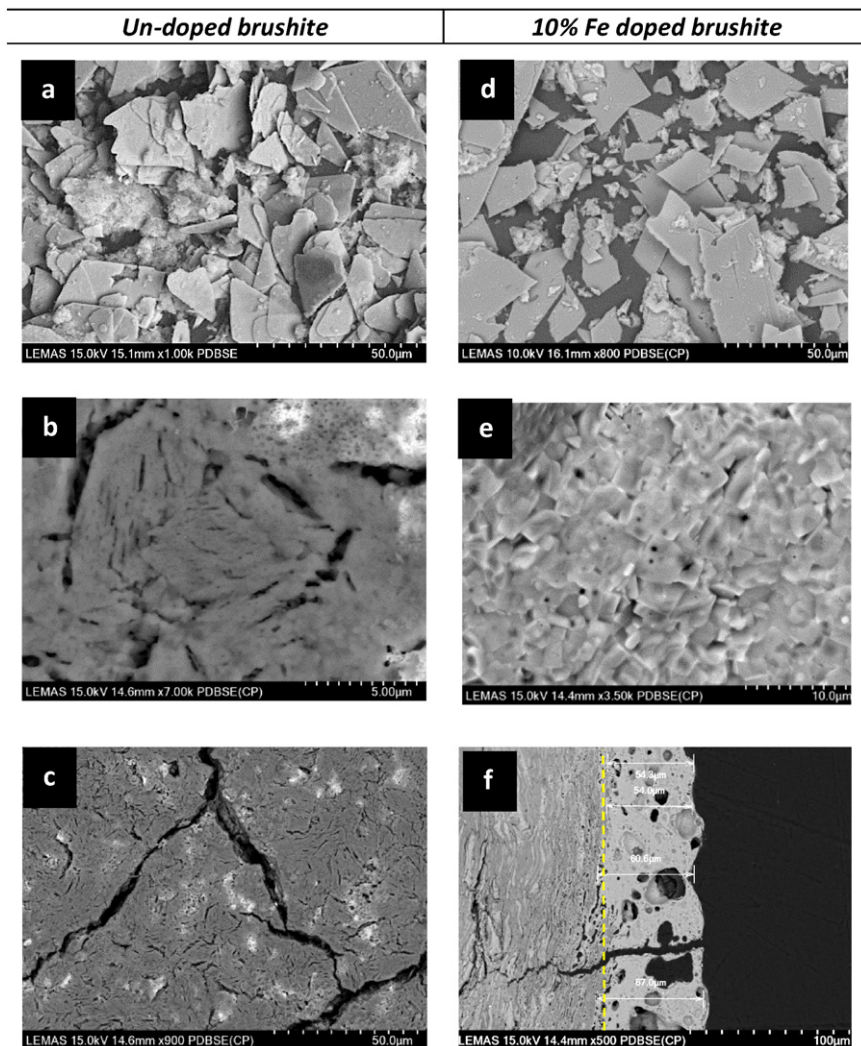
Fig. 6. SEM images showing the morphology of un-doped (a, b, c) and Fe doped (d, e, f) brushite before (a, d) and after (b, c, e, f) laser irradiation.
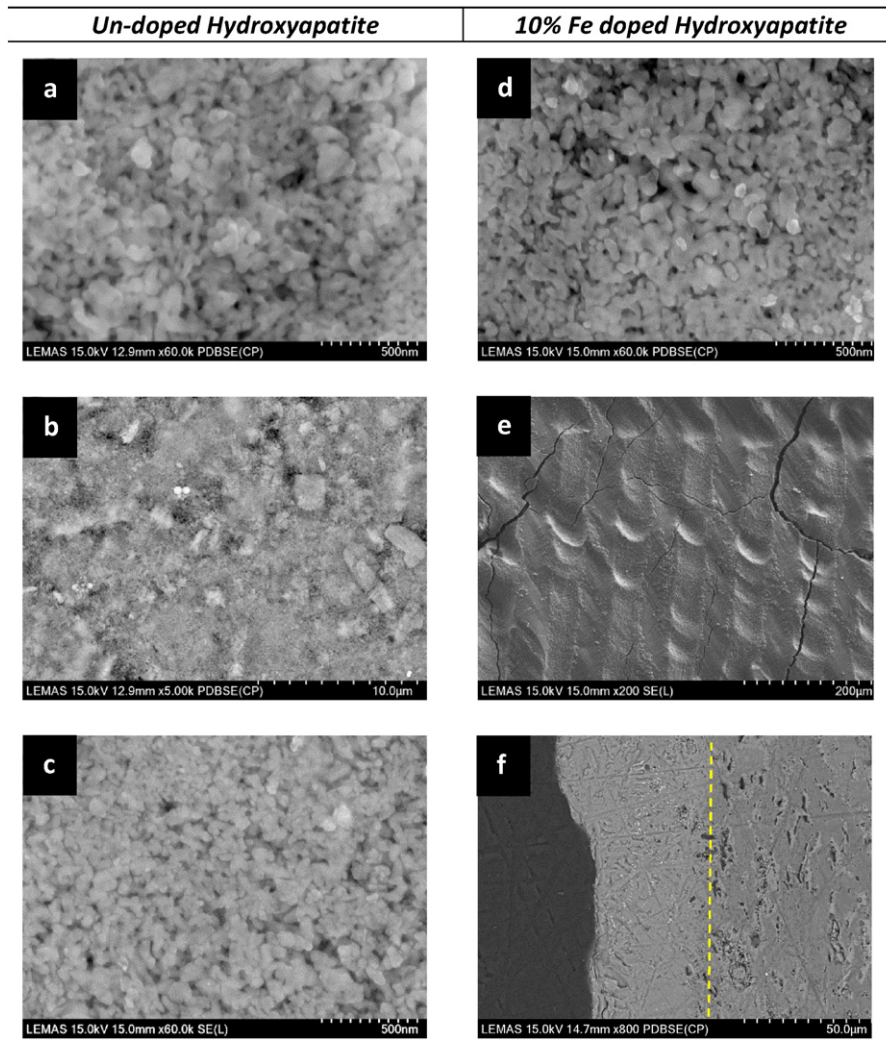
Fig. 7. SEM images showing the morphology of un-doped (a, b, c) and Fe doped (d, e, f) hydroxyapatite before (a, d) and after (b, c, e, f) laser irradiation.

surface is evident in the irradiated material (Fig. 7e and f), compared to the loosely packed nano-crystals of the starting material (Fig. 7d). The irradiated microstructure has reduced porosity and also shows limited cracking, suggesting that adhesion between the layers may have reduced the overall expansion coefficient differences. A SEM image of the cross-section of the HAP-Fe sample is presented in Fig. 7f, and the depth of dense sintering is 40–45 μm.

3.2. Heat dissipation

Measurements of surface temperature of the mineral phase during laser irradiation are nontrivial, since very high spatial and time resolution are needed to obtain reliable data. To investigate heat dissipation on the surface of the sample we have adopted an alternative approach, based on the assumption that the irradiation has induced thermal phase transformations of brushite (Fig. 2 and Table 2). The resulting

compositional differences between the brushite and the newly formed monetite and pyrophosphate phases are significant, particularly in terms of oxygen content since each transformation is accompanied by the removal of water molecules (Table 3). We have used SEM analysis to identify and focus on the areas that are visibly altered and yet have not been directly irradiated (as is defined by the first laser track). For these areas we can assume that transformations are heat induced and the resulting loss of water of crystallisation changes the overall atomic mass, yielding sufficient atomic number contrast between the transformed phases in the backscattered SEM image (e.g. for the un-doped brushite Fig. 8), three different un-irradiated zones at the surface of the sample can be identified. In order to measure the oxygen content of each of these zones a EDX line scan analysis was carried out (Fig. 9). Starting from the dark region (zone 1), furthest away from the irradiated area, it is evident that the average O content is around 52 wt%. Traversing towards the irradiated area and into zone 2, the average analyzed oxygen content has dropped to 46 wt%, and finally in zone 3, the region immediately adjacent to the irradiated area, the analyzed oxygen content is 39 wt% (Fig. 9). Thus we can suggest that in zone 1 the dominant phase is brushite (expected O content is 57.5 wt%), in zone 2 monetite (expected O content is 47.4 wt%) and in zone 3 pyrophosphate (expected O content is 44.4 wt%). Since there are no compositional differences between the three forms of pyrophosphate, it is difficult to distinguish each in a mixed microstructure such as in zone 3. However, based on the X-ray diffraction and thermal analyses,

Table 3
Theoretical composition of brushite, monetite and pyrophosphate.

	Brushite		Monetite		Pyrophosphate	
	A%	wt%	A%	wt%	A%	wt%
Oxygen	75	**57.5**	66.7	**47.4**	64	**44.1**
Calcium	12.5	23.9	16.7	29.6	18	31.5
Phosphate	12.5	18.6	16.7	23.0	18	24.4
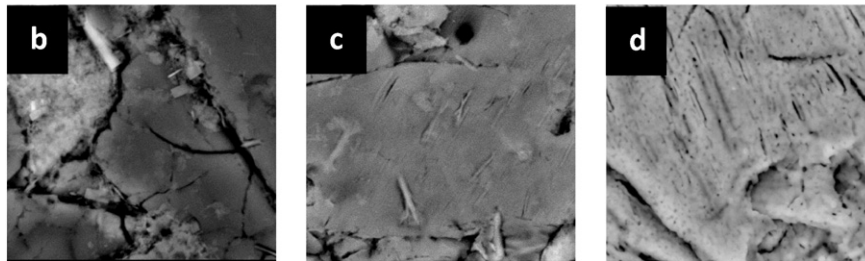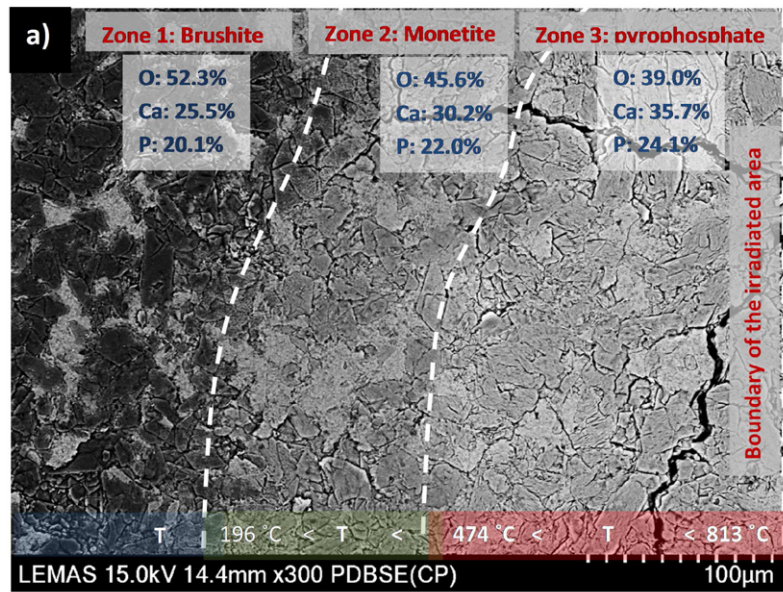
Fig. 8. Examination of the different mineral reaction zones beyond the boundary of the directly irradiated region of a brushite pellet (DCPD-UN); a) identification of each zone by measurement of average oxygen concentration (by EDX quantification) and estimated temperature at the zone boundaries; b) morphology of the crystals in zone1; c) morphology of the crystals in zone 2; d) morphology of the crystals in zone 3.

discussed above, we can assume that at the boundary of the irradiated region we have the β-form. The corresponding phase in each zone can be also verified by the morphology of the crystals. The morphology of the crystals in zone 1 (Fig. 8b) is similar to the non-irradiated brushite (Fig. 6a). In zone 2 although the crystals retain the original platelet
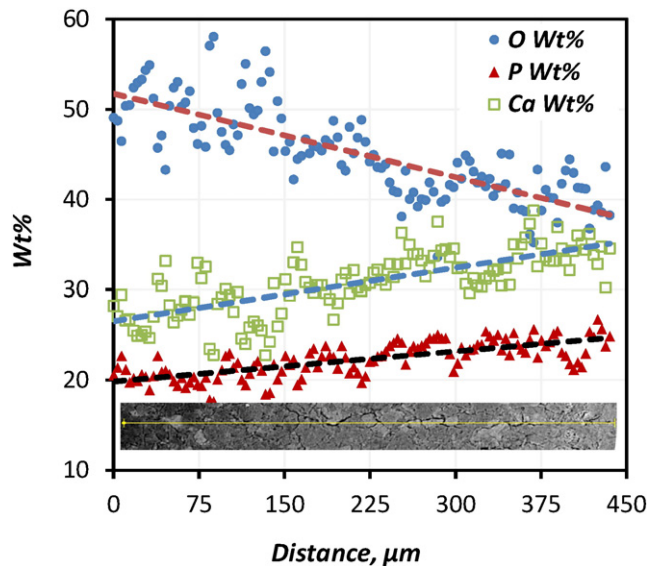
Fig. 9. Energy dispersive X-ray spectroscopy line scan across the three zones identified on an irradiated region of the Brushite pellet, showing the continuous change in elemental content across the zones.

morphology of brushite, the removal of water of crystallisation on transformation to monetite leaves only some residual porosities (Fig. 8c). In zone 3 (Fig. 8d), the crystals have comparable porous, morphologies to the pyrophosphate in the irradiated region in Fig. 6b, c.

After identifying the dominant mineral phase present in each zone and combining with the transformation temperatures measured by the thermal analysis (Table 2), we can estimate the temperature at the boundaries of each zone (Fig. 8a). For the Fe^{3+}-doped brushite samples, a similar phase transformation based analysis was carried out. As in the case of the un-doped brushite, the three zones of unique phases were characterized. However, in this case there is also evidence for a fourth zone which is identified by the apparent difference between the densified crystals and the rest of the material (Fig. 7c). A heat dissipation curve may be obtained when these phase transformation-temperature data are correlated with the distance of the zones from the boundary of the irradiated region (Fig. 10). The width of each phase boundary zone is averaged over 8 different areas with a measured variance of 5 to 10 μm, which then yields 5% error bars (Fig. 10). What is quite intriguing is that in spite of such broad assumptions for estimating the zonal temperatures in each of the two materials, the plotted curves show linear behaviour, consistent with Fourier's law for one dimensional heat conduction problems [25].

3.3. Discussion

The characterisation of the fs-pulsed laser irradiated materials demonstrates that significant volume sintering and densification have been achieved only in the Fe^{3+}-doped minerals. During irradiation, the un-doped brushite has transformed into β-pyrophosphate without any obvious evidence of crystal growth or sintering (see Figs. 3a and 6)
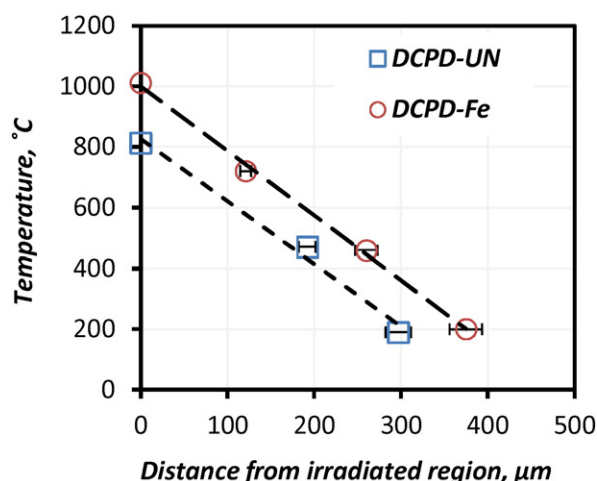
Fig. 10. Heat dissipation curve for the un-doped (DCPD-UN) and Fe-doped brushite (DCPD-Fe) pellets. Data points are averages of 8 areas from for each sample, error bars of 5% uncertainty indicate the range of the measurements.

and the HAP-UN sample remained largely unaltered after laser irradiation (as shown in Figs. 3b and 7a–c). In comparison the Fe-doped materials exhibit a very clearly transformed phase and microstructure (Figs. 6d–f and 7d–f). The different sintering and densification behaviour of the doped and un-doped materials stems from two factors, discussed below.

a) Doping with iron increases the optical absorption of the minerals at 1045 nm. The fraction of the laser energy which transforms to heat during the irradiation of the samples can be described by the linear energy absorption rate (S) which results from the beam-material interaction [26]. As presented in Eq. (3), S is a function of the laser energy flux (J), the pulse duration (t_p), the radiation penetration depth (δ) and the material's reflectivity (R). Since the irradiation parameters have been constant for all the experiments, reflectivity is the only parameter that differs from sample to sample. By calculating S for the three cases it can be shown that the energy absorption rate is 4 times higher for the HAP-Fe and 2 times for the DCPD-Fe compared to the DCPD-UN. Thus it is obvious that although the incident irradiation energy was identical for all the samples, much higher absorption and thus surface temperatures are expected for the Fe^{3+}-doped materials, increasing the chances of achieving sintering and densification.

$$S = 0.94 \frac{(1-R)J}{t_p \delta} \exp\left(-\frac{x}{\delta} - \frac{1.992(t-2t_p)}{t_p}\right) \qquad (3)$$

Based on the phase transformations observed for the DCPD-UN and DCPD-Fe pellets the surface temperatures reached during irradiation have been estimated to be between 800 and 1000 °C. Since the total exposure time of each point of the surface is 0.3 s we can estimate that the heating rates during exposure to the laser beam range from 2600 to 3300 °C/s. At first glance these high temperatures are not an encouraging finding for clinical use, especially considering that the motivation of this work is the demonstration of a safe way to achieve direct sintering on hard tissues. Even for short exposure times, temperatures up to only 40–42 °C could be considered absolutely safe for soft human tissues [27]. However, by extrapolating the heat dissipation curves (Fig. 10) to a temperature of 40 °C we find that the distance of the 'safe' region from the irradiation area is about 380 μm for the DCPD-UN and 450 μm for the DCPD-Fe. These distances are extremely short and we can therefore conclude that the rise in temperature due to laser irradiation is actually very localised.

b) As well as the presence of Fe^{3+} in each mineral lattice influencing the optical absorption of the material, the iron based dopants are responsible for the formation of lower melting point phases e.g.

the iron-calcium pyrophosphate having a reduced $T_{melting}$ of 1012 °C (Table 2). Assuming substitutional doping of Fe for Ca (supported in part by the reduced lattice volume of the iron doped material identified by XRD; Fig. 2), then the difference in the cationic charge and size between Fe^{3+} (0.07 nm) and Ca^{2+} (0.1 nm) may give rise to increased numbers of vacancies and point defects which are critical for lattice-diffusion-controlled sintering [24].

In summary, high laser radiation absorptivity and the difference in cationic characters of Ca^{2+} and Fe^{3+} are apparently the driving factors for enhanced sintering in iron-doped minerals.

Another important finding of this work are the final phases produced by laser irradiation. The formation of the β-pyrophosphate could be promising for applications related to bone regeneration. Although at the moment hydroxyapatite is the most widely used biomaterial for the construction of bone scaffolds and other regenerative devices, it was found that HAP blocks are non-biodegradable even after long periods of implantation [14]. Recent studies have demonstrated the importance of pyrophosphate ions to the mineralisation of bone (e.g. [28]). Grover et al. [15] suggested that enzymatic action accelerates dissolution of the inorganic pyrophosphate ions causing a simultaneous loss of mineralisation and a localised rise in ion saturation with respect to HA and as a result the presence of pyrophosphate in say a cement matrix can stimulate bone mineralisation and healing. Thus, pyrophosphate coatings of small bone defects potentially could act as a substrate for enzymes that trigger specific biological reactions in favour of bone mineralisation and healing [15].

Another factor which renders the DCPD-Fe sintered material advantageous for bone healing applications is the open porosity and microcracking observed compared to the compact layer of the irradiated HAP-Fe material. It is widely known that porosity favours healthy ingrowth of osteoblasts and that the pore interconnection size is critical during bone healing. In many cases a pore size of 100 μm is considered a requirement for healthy ingrowth but it has been also reported that even for pore sizes as small as 40 and 50 μm (the size of the pores found in the sintered DCPD-Fe) there is evidence for mineralised bone ingrowth ([29,30]).

Finally, while there is considerable focus on the manufacturing of tissue scaffolds and bioactive glasses utilising continuous wave lasers (e.g. [6,7,8,9,10,31]), the novelty of the present work is the demonstration of surface sintering of calcium phosphate based biomaterials directly by a femtosecond laser. To the best of our knowledge sintering of calcium phosphate materials with femtosecond lasers has never been demonstrated before. In the work of Symietz et al. [11] a femtosecond laser, operating at energy densities between the ablation thresholds of the Ti alloy (0.1 J/cm^2) and the calcium phosphate materials (0.4 J/cm^2), have been utilised to melt a thin layer of the Ti surface to promote binding of the calcium phosphate particles without altering them. While in the work of Elmadani et al. [13] a 2.5 GHz repetition rate femtosecond laser, emitting at 1525 nm, was used to demonstrate the densification of a photosensitive Er-doped brushite/monetite mixture and the bonding with dental enamel. In both the aforementioned works and unlike that presented here, there is indication of sintering due to thermal effects and no phase transformations of the initial material have been identified following irradiation. Thus, our results demonstrate the potential to resurface hard tissue (such as bone or enamel) by pulsed laser sintering on a new mineral layer without significant thermal transformation of the underlying tissue. This could be a complementary surface restoration procedure to current bone repair and regeneration approaches (e.g. [32,33]).

4. Conclusions

In the present work we investigated the laser sintering of calcium phosphate biomaterials with the use of a femtosecond pulsed laser operating at 1045 nm. The most important outcomes of our investigations can be concluded as the following:

- Laser induced sintering and densification has been achieved only for the Fe^{3+}-doped calcium phosphate materials. Undoped HAP crystals remained largely unchanged or unreacted after laser irradiation, whereas, undoped brushite transformed into pyrophosphate without any indications of crystal growth or densification.
- Doping with Fe^{3+}-ions resulted in the characteristic thermal phase transformation temperatures of brushite to shift to lower temperatures, thereby promoting densification and sintering (e.g. the transformation temperature for the β-pyrophosphate to α-form has been reduced by 212 °C by Fe-doping while, the melting point reduced by 108 °C).
- Doping with Fe^{3+}-ions resulted in increased laser absorption by the materials. Thus, pulsed laser irradiation of the Fe^{3+}-doped brushite resulted in transformation to a continuous but highly porous β-pyrophosphate phase. These types of porous materials might have applications related to bone regeneration (e.g. coating or construction of scaffolds) where porosity and biodegradability are critical. Whereas, irradiation of Fe^{3+}-doped HAP produces a dense layer of enamel like material that would be useful for acid eroded enamel restoration and for treating small bone defects.
- Analysis of heat affected transformation zones on irradiated brushite samples enables estimation of the surface temperature and heat dissipation curves during irradiation. A temperature rise of 1000 °C at the area of irradiation (30 μm diameter) was evident but this temperature rise is localised, as it is estimated to drop to 40 °C within 500 μm from the irradiation zone i.e. surrounding areas remain relatively unaffected by the irradiation process.

Overall, this work demonstrates the bonding of a new calcium phosphate based mineral layer to existing surfaces by pulsed laser sintering. Such an approach could be used to restore or reconstruct hard tissue defects (in bone or enamel) without significant thermal transformation of the underlying tissue. Raw data repository: http://doi.org/10.5518/48.

Acknowledgements

References

[1] E. Abrahams, M. Silver, The history of personalised medicine, in: E. Gordon, S. Koslow (Eds.), Integrative Neuroscience and Personalised Medicine, New York: NY: Oxford University Press 2010, pp. 3–16.

[2] C.T. Laurencin, L.S. Nair, Nanotechnology and Regenerative Engineering: The Scaffold, Taylor & Francis, Second edition, 2014.

[3] M.H. Niemz, Laser-Tissue Interactions: Fundamentals and Applications, Springer, 2007.

[4] G.M. Hale, M.R. Querry, Optical constants of water in the 200-nm to 200-μm wavelength region, Appl. Opt. 12 (1973) 555–563.

[5] P. Fischer, N. Karapatis, V. Romano, R. Glardon, H.P. Weber, A model for the interaction of near-infrared laser pulses with metal powders in selective laser sintering, Appl. Phys. A Mater. Sci. Process. 74 (2002) 467–474.

[6] J. Zhou, C. Gao, P. Feng, T. Xiao, C. Shuai, S. Peng, Calcium sulfate bone scaffolds with controllable porous structure by selective laser sintering, J. Porous. Mater. 22 (2015) 1171–1178.

[7] J. Liu, C. Gao, P. Feng, S. Peng, C. Shuai, Selective laser sintering of β-TCP/nano-58S composite scaffolds with improved mechanical properties, Mater. Des. 84 (2015) 395–401.

[8] E.N. Antonov, V.N. Bagratashvili, M.J. Whitaker, J.J.A. Barry, K.M. Shakesheff, A.N. Konovalov, et al., Three-dimensional bioactive and biodegradable scaffolds fabricated by surface-selective laser sintering, Adv. Mater. (Deerfield Beach, Fla) 17 (2004) 327–330.

[9] E.N. Antonov, S.M. Barinov, I.V. Vakhrushev, V.S. Komlev, V.K. Popov, A.Y. Fedotov, et al., Selective laser sintering of bioactive composite matrices for bone tissue engineering, Inorg. Mater. Appl. Res. 6 (2015) 171–178.

[10] K.P. O'Flynn, K.T. Stanton, Laser sintering and crystallization of a bioactive glass-ceramic, J. Non-Cryst. Solids 360 (2013) 49–56.

[11] C. Symietz, E. Lehmann, R. Gildenhaar, J. Krüger, G. Berger, Femtosecond laser induced fixation of calcium alkali phosphate ceramics on titanium alloy bone implant material, Acta Biomater. 6 (2010) 3318–3324.

[12] C. Symietz, E. Lehmann, R. Gildenhaar, R. Koter, G. Berger, J. Krüger, Fixation of bioactive calcium alkali phosphate on Ti6Al4V implant material with femtosecond laser pulses, Appl. Surf. Sci. 257 (2011) 5208–5212.

[13] E. Elmadani, A. Jha, T. Perali, C. Jappy, D. Walsh, C. Leburn, et al., Characterization of rare-earth oxide photoactivated calcium phosphate minerals for resurfacing teeth, J. Am. Ceram. Soc. 95 (2012) 2716–2724.

[14] F.H. Lin, C.C. Lin, C.M. Lu, H.C. Liu, J.S. Sun, C.Y. Wang, Mechanical properties and histological evaluation of sintered β-Ca$_2$P$_2$O$_7$ with Na$_4$P$_2$O$_7$·10H$_2$O addition, Biomaterials 16 (1995) 793–802.

[15] L.M. Grover, A.J. Wright, U. Gbureck, A. Bolarinwa, J. Song, Y. Liu, et al., The effect of amorphous pyrophosphate on calcium phosphate cement resorption and bone generation, Biomaterials 34 (2013) 6631–6637.

[16] Elliott JC, Chapter 1 - general chemistry of the calcium orthophosphates, in: Elliott JC (Ed.), Studies in Inorganic Chemistry, Elsevier 1994, pp. 1–62.

[17] F. Tamimi, Z. Sheikh, J. Barralet, Dicalcium phosphate cements: brushite and monetite, Acta Biomater. 8 (2012) 474–487.

[18] A. Manchon, M. Hamdan Alkhraisat, C. Rueda-Rodriguez, J.C. Prados-Frutos, J. Torres, J. Lucas-Aparicio, et al., A New Iron Calcium Phosphate Material to Improve the Osteoconductive Properties of a Biodegradable Ceramic: A Study in Rabbit Calvaria, Biomed. Mater. (Bristol, England) 10 (2015) 055012.

[19] A.O. McIntosh, W.L. Jablonski, X-ray diffraction powder patterns of calcium phosphates, Anal. Chem. 28 (1956) 1424–1427.

[20] N. Webb, The crystal structure of β-Ca$_2$P$_2$O, Acta Crystallogr. 21 (1966) 942–948.

[21] J.-J. Bian, D.-W. Kim, K.-S. Hong, Phase transformation and sintering behavior of Ca$_2$P$_2$O$_7$, Mater. Lett. 58 (2004) 347–351.

[22] K. Tõnsuaadu, K. Gross, L. Plūduma, M. Veiderma, A review on the thermal stability of calcium apatites, J. Therm. Anal. Calorim. 110 (2012) 647–659.

[23] B.I. Lazoryak, V.A. Morozov, A.A. Belik, S.S. Khasanov, V.S. Shekhtman, Crystal structures and characterization of Ca$_9$Fe(PO$_4$)$_7$ and Ca$_9$FeH$_{0.9}$(PO$_4$)$_7$, J. Solid State Chem. 122 (1996) 15–21.

[24] S.-J.L. Kang, Sintering - Densification, Grain Growth, and Microstructure, Elsevier, 2005.

[25] J.H. Lienhard, A Heat Transfer Textbook: Prentice Hall PTR, 1981.

[26] D.Y. Tzou, K.S. Chiu, Temperature-dependent thermal lagging in ultrafast laser heating, Int. J. Heat Mass Transf. 44 (2001) 1725–1734.

[27] P.S. Yarmolenko, E.J. Moon, C. Landon, A. Manzoor, D.W. Hochman, B.L. Viglianti, et al., Thresholds for thermal damage to normal tissues: an update, Int. J. Hyperth. Off. J. Eur. Soc. Hyperth. Oncol. North Am. Hyperth. Group 27 (2011) 320–343.

[28] S.M. Naga, M. Awaad, H.F. El-Maghraby, A.M. El-Kady, Biological performance of calcium pyrophosphate-coated porous alumina scaffolds, Int. J. Appl. Ceram. Technol. 11 (2014) 1–11.

[29] J.J. Klawitter, J.G. Bagwell, A.M. Weinstein, B.W. Sauer, An evaluation of bone growth into porous high density polyethylene, J. Biomed. Mater. Res. 10 (1976) 311–323.

[30] R.E. Holmes, Bone regeneration within a coralline hydroxyapatite implant, Plast. Reconstr. Surg. 63 (1979) 626–633.

[31] S. Duan, P. Feng, C. Gao, T. Xiao, K. Yu, C. Shuai, et al., Microstructure evolution and mechanical properties improvement in liquid-phase-sintered hydroxyapatite by laser sintering, Materials 8 (2015) 1162.

[32] J. Henkel, M.A. Woodruff, D.R. Epari, R. Steck, V. Glatt, I.C. Dickinson, et al., Bone regeneration based on tissue engineering conceptions — a 21st century perspective, Bone Res. 1 (2013) 216.

[33] A.R. Amini, C.T. Laurencin, S.P. Nukavarapu, Bone tissue engineering: recent advances and challenges, Crit. Rev. Biomed. Eng. 40 (2012) 363–408.